A Tool for Super-Resolving Multimodal Clinical MRI

Mikael Brudfors[a,*], Yaël Balbastre[a], Parashkev Nachev[b], John Ashburner[a]

[a] *Wellcome Centre for Human Neuroimaging, University College London, London WC1N 3BG, UK*
[b] *Institute of Neurology, University College London, London WC1N 3BG, UK*

Abstract

We present a tool for resolution recovery in multimodal clinical magnetic resonance imaging (MRI). Such images exhibit great variability, both biological and instrumental. This variability makes automated processing with neuroimaging analysis software very challenging. This leaves intelligence extractable only from large-scale analyses of clinical data untapped, and impedes the introduction of automated predictive systems in clinical care. The tool presented in this paper enables such processing, via inference in a generative model of thick-sliced, multi-contrast MR scans. All model parameters are estimated from the observed data, without the need for manual tuning. The model-driven nature of the approach means that no type of training is needed for applicability to the diversity of MR contrasts present in a clinical context. We show on simulated data that the proposed approach outperforms conventional model-based techniques, and on a large hospital dataset of multimodal MRIs that the tool can successfully super-resolve very thick-sliced images. The implementation is available from `https://github.com/brudfors/spm_superres`.

Keywords: Generative modelling, Super-resolution, MRI, Clinical data, Multi-channel total variation

1. Introduction

Automated analysis of magnetic resonance imaging (MRI) data enables studies of the brain that would be either very time consuming, or simply not possible, if performed manually. These automated methods can be used to, *e.g.*, investigate differences in tissue composition between groups of subjects (Ashburner and Friston, 2000), examine changes over time due to ageing and neurodegenerative disorders (Reuter et al., 2012), make predictions between healthy and diseased patients (Klöppel et al., 2008) or delineate to a clinician the location of some pathology (Kamnitsas et al., 2017). Many neuroimaging software packages used for such analysis, *e.g.*, SPM (Ashburner and Friston, 2005), FSL (Zhang et al., 2001) and FreeSurfer (Fischl et al., 2004), are tailored for small, almost isotropic voxels, with high contrast between grey matter (GM) and white matter (WM). As they require more time and high field strengths, these types of features are mostly found in images acquired in a controlled, research context.

MR images acquired in a clinical setting have much greater variability than their research counterparts, as clinicians do not target reproducibility, but aim at maximising sensitivity to a suspected pathology. This variability can be disentangled into instrumental and biological. The instrumental variability stems from: (1) clinicians favouring speed over volume resolution and therefore typically acquiring images with high in-plane resolution, but fewer and thicker slices; and (2), the scans being acquired across a diverse set of MR sequences, sensitive to different tissue properties and, therefore, different pathologies. On the other hand, the biological variability relates to the diverse morphological variability in patient brains due to different clinical conditions, as well as a wide age distribution. All in all, this leads to a huge diversity in clinical MRI data. A comparison between MR images acquired in a research and a clinical context is shown in Figure 1. Applying automated analysis pipelines, successfully, to images acquired in a routine clinical setting is much more challenging than applying them to research images. For example, the aforementioned software packages were recently evaluated at the task of brain GM and WM volume estimation from isotropic and anisotropic volumes acquired in the same subjects, and results were improved by several percentage points when isotropic volumes were used over thick-sliced ones (Adduru et al., 2017).

Conversely, researchers interested in applying automated analysis methods to MR data trade speed for resolution and therefore tend to acquire high-resolution (HR) volumetric images. This makes large-scale studies, with thousands of subjects, difficult to perform due to the expense of scanning with such parameters. For example, UK BioBank took a decade of planning and acquisition (Ollier et al., 2005), at a cost of more than £60 million (Palmer, 2007). However, such studies can provide great opportunities for making new discoveries about the brain (Miller et al., 2016; Smith and Nichols, 2018; Van Essen et al., 2013). Clinical data does not have this problem,

*Corresponding author: Mikael Brudfors
`mikael.brudfors.15@ucl.ac.uk`

as huge amounts of population-representative[1] scans exist (Roobottom et al., 2010), accumulated over years of clinical service. Furthermore, these scans are available for research at cost neutrality and have a much higher prevalence of pathology, which is of interest if disease is to be investigated rather than normality.

Commonly, for analyses that require isotropic voxels, thick-sliced volumes are upsampled using simple interpolation, even though it can introduce artefacts such as aliasing (Aganj et al., 2012) and bias subsequent analyses. In this paper we propose a method for reconstructing HR images with isotropic voxels from multimodal, low-resolution (LR) clinical scans, based on a principled generative model. Carefully crafted generative models have been shown to generalise well in the case of medical image segmentation (Ashburner and Friston, 2005; Fischl et al., 2004; Zhang et al., 2001), and we here developed such a model for clinical MRI super-resolution. The objective of our model is to merge information that is distributed across all MR scans of a patient, in order to generate closer-to-research quality images from clinical scans. Reconstructing isotropic HR images in such a way could in turn better enable the aforementioned large-scale studies. The multi-sequence capability of the proposed model stems from a cross-channel[2] functional that has been studied extensively in the computer vision community; in MRI, for parallel image reconstruction (Chatnuntawech et al., 2016) and recently introduced for multimodal super-resolution (Brudfors et al., 2018).

The model-based approach we propose in this paper is data agnostic and does not require any complex learning. Learning a representative distribution of the large number of sequences used in clinical MR imaging is extremely challenging and would make the model much less general. Having to train a model anew, each time a new combination of MR contrasts is encountered, or a different scaling factor is needed, would make a general tool much more difficult to develop.

We show on a large number of patient scans that the model is capable of super-resolving very thick-sliced clinical MRIs (≈6.5 mm), with missing fields of view. To ensure good generalisability, all model parameters were estimated in a principled way. Our implementation is publicly available, and can be used by researchers interested in analysing routine clinical MR data. The implementation is available from `https://github.com/brudfors/spm_superres`, we intend to shortly incorporate it into the SPM12 software[3].

[1] Not the general population – rather the population who are likely to have had strokes, tumours, etc.

[2] We consider the different MR contrasts acquired in a patient as being equivalent to colour channels in computer vision (*e.g.*, RGB).

[3] `www.fil.ion.ucl.ac.uk/spm/software/spm12`

2. Super-Resolution in Brain MRI

In image processing, the task of improving the resolution of an image after it has been acquired is known as super-resolution[4]. There are two cardinal ways of super-resolving: the first is to combine information from a multiplicity of images of the same subject, the second is to introduce guidance from a population of other subjects. For both these methods it common to use some kind of inductive bias given mathematically or conceptually, *e.g.*, regularisation.

Super-resolution was first studied in the computer vision field in the early 80s and has since grown to become an active area of research using tools from, *e.g.*, inverse problems and machine learning (Huang and Yang, 2010; Yue et al., 2016). In the early 2000s, super-resolution found applications in the medical imaging community, in particular for brain MRI (Van Reeth et al., 2012). This was partly due to multi-LR super-resolution's dependency on exact image alignment, where for brain imaging it is possible to obtain good alignment simply by rigid registration. It was furthermore shown that super-resolution improved resolution and signal-to-noise ratio favourably, compared with direct HR acquisition (Plenge et al., 2012).

The earliest works investigating super-resolution applied to brain MR images, defined an observation model that did not take into account multiple MR contrasts, but rather specified how a set of LR images, of the same contrast, were generated from a HR image (Greenspan et al., 2001; Peled and Yeshurun, 2001). The basic idea was that it should be more beneficial (with respect to the trade-off between acquisition time and signal-to-noise ratio), to acquire multiple LR images, and then combining them using super-resolution, than acquiring one HR image. The observation model was constructed by linear operations (shift, down-sampling, blurring) and additive Gaussian noise. A maximum likelihood (ML) estimate of the unknown HR image could then be found by a gradient descent style algorithm. Limited in handling scans only of the same orientations, but with subpixel offsets, Shilling et al. (2009) extended the methods based on observation models to handle multiple LR images, of different slice-select directions. The work of Poot et al. (2010) subsequently generalised this approach to images not necessarily rotated around a common frequency encoding axis, allowing for any slice orientation. They additionally solved the optimisation problem efficiently using a conjugate gradient algorithm.

The ML methods were quickly extended to include some form of regularisation via maximum a posteriori (MAP) estimation, in order to reduce the ill-posedness of the solution, as well incorporating prior knowledge (*e.g.*, neigh-

[4] The term super-resolution can also be used to describe techniques attempting to transcend the diffraction limit of an optical system, *e.g.*, super-resolution microscopy.

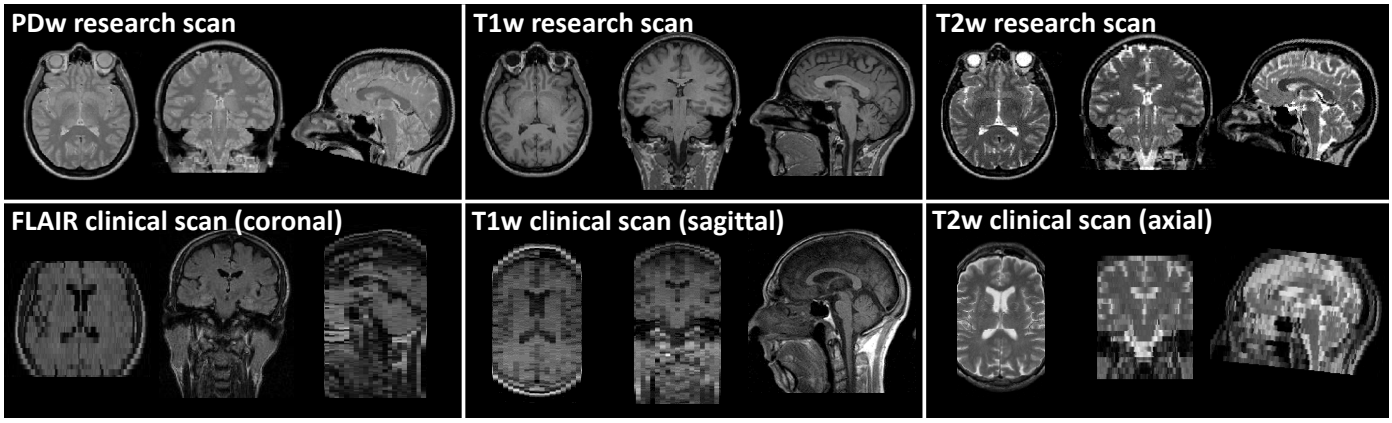

Figure 1: Comparing research and clinical MRI. The top row shows PD-weighted (PDw), T1-weighted (T1w) and T2-weighted (T2w) MR images of a subject from the high-resolution IXI dataset, which is used in the simulated results section of this paper. The three scans have close to 1 mm isotropic voxels. The bottom row shows FLAIR, T1w and T2w MR images of a subject from the clinical dataset we use in our evaluation. These subject's scans have thick-slices (6.5 mm), with different slice-select directions, and partial brain coverage.

bouring voxels should look similar). The work of Peeters et al. (2004), Kainz et al. (2015) and Rousseau et al. (2010b) did so using edge-preserving functionals, such as the Huber function or anisotropic diffusion, to regularise their solutions, while Zhang et al. (2008) and Poot et al. (2010) used the Euclidean norm of the image gradients. In Bai et al. (2004) a Markov random field was used, and in Shi et al. (2015) two sorts of regularisation were combined: the edge-preserving total variation and a low-rank term that enabled utilisation of information throughout the image. Also Tourbier et al. (2015) used total variation as a regulariser, with an adaptive regularisation scheme. Besides including some sort of regularisation in the objective function, replacing its mean-squared error norm has also been explored, with the aim of increased robustness to incorrect noise models (Gholipour et al., 2010).

The methods discussed up until this point are non-optimal for processing clinical MRIs, as they assume multiple LR images of the same contrast and hence do not utilise the fact that routine clinical scans often are of different contrasts. A method utilising information from a HR reference image of a different contrast was first proposed by Rousseau et al. (2010a). The super-resolved image was obtained by iteratively denoising the current estimate of the super-resolved image with a patch-based technique, using the HR image as a reference, and then solving an optimisation problem, where the denoised image regularised the solution. The patch-based work of Manjón et al. (2010a) used the information from a HR reference in a similar way, but instead of solving for the super-resolved image in an optimisation setting, they used an iterative reconstruction-correction scheme. Another patch-based approach estimated weights from a HR image of a given contrast and then regressed a HR image from a LR image with a different contrast (Zheng et al., 2017). Numerous other works on super-resolving MRIs have used these patch-based approaches, utilising the pattern redundancy present in image patches (Coupé et al., 2013; Jog et al., 2014; Manjón et al., 2010b; Plenge et al., 2013). However, although these methods enable super-resolving across MR channels, they require access to HR data. Such data is seldom available in a clinical setting. To mitigate this problem, methods have been developed that utilises the property that clinical MR images are inherently anisotropic to learn a regression between LR and HR images (Jog et al., 2016; Zhao et al., 2018); however, using only a single contrast.

Data-driven (or learning-based) methods have also been thoroughly investigated for the task of super-resolving brain MRIs. These methods aim at learning a LR to HR mapping from training data. One of the first such methods was proposed by Rueda et al. (2013), using sparse dictionary learning. Also, regression-based techniques have been explored, such as patch-based random forest regression (Alexander et al., 2014; Sindel et al., 2018). Convolutional neural networks is another class of supervised methods that has gained interest in MRI super-resolution (Cengiz et al., 2017; Pham et al., 2017; Tanno et al., 2017). Deep generative models have also been used to directly learn a LR to HR distribution for super-resolution recovery (Chen et al., 2018). To combat the fact that HR training data is difficult to obtain, Dalca et al. (2018) proposed a generative model for sparse image patches, where LR clinical scans were used as training data. They additionally dealt with missing data in an elegant way. However, to the best of our knowledge, there is not yet a learning-based super-resolution tool useable without the need for training anew, when faced with unseen contrasts.

3. Methods

Compared with some of the super-resolution approaches mentioned in the previous section, the model we propose here it multimodal, and does not require any complex learning, nor any HR reference data. We additionally avoid any learning from training data with the hope of

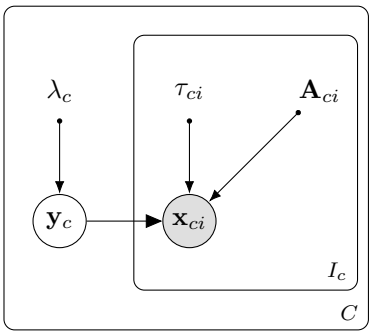

Figure 2: Graphical model of the joint probability distribution in equation (1). Random variables are in circles, observed variables are shaded, plates indicate replication. There are C unknown HR images ($\mathbf{y}_c$) and I_c observed LR images ($\mathbf{x}_{ci}$) for each c. Model parameters are dotted and are the Gaussian noise precisions τ_{ci}, projection matrices $\mathbf{A}_{ci}$, and regularisation parameters λ_c.

improved generalisability when applying the model to diverse clinical MR scans. The model instead relies on the definition of a joint distribution of a patient's multimodal MR images. A generative model that integrates multimodal images requires a component that relates signal across the various modalities. Here, this component is a novel prior in the context of MRI super-resolution, which promotes combining image information distributed across a patient's MR images. In this section, we consider that each MR contrast (*e.g.*, T1w, T2w, PDw) constitutes one channel of a multi-channel volume. When multiple images of the same contrast are acquired, they are considered as multiple noisy observations of the same channel.

3.1. The Generative Model

The model assumes that each LR image is generated by selecting thick slices, arbitrarily rotated and/or translated, from a HR image, with the addition of random noise. This assumption can be written as a conditional probability distribution known as the data likelihood. We also assume that each HR image is the result of a random process, characterised by a probability distribution known as the prior. This generative model is formalised by the joint probability distribution:

$$p(\boldsymbol{\mathcal{X}}, \mathbf{Y}) = \underbrace{p(\boldsymbol{\mathcal{X}} \mid \mathbf{Y})}_{\text{likelihood}} \underbrace{p(\mathbf{Y})}_{\text{prior}} = \prod_{c=1}^{C} \prod_{i=1}^{I_c} p(\mathbf{x}_{ci} \mid \mathbf{y}_c)\; p(\mathbf{Y}), \tag{1}$$

where $\mathbf{Y} = \{\{\mathbf{y}_c\}_{c=1}^{C} \mid \mathbf{y}_c \in \mathbb{R}^N\}$ denotes the unknown HR images of C different channels and $\boldsymbol{\mathcal{X}} = \{\{\mathbf{X}_c\}_{c=1}^{C} \mid \mathbf{X}_c = \{\mathbf{x}_{ci}\}_{i=1}^{I_c} \mid \mathbf{x}_{ci} \in \mathbb{R}^{N_{ci}}\}$ a set of LR images. The variable I_c is the number of observed LR images of channel c, N is the number of voxels in the HR images, and N_{ci} is the number of voxels in the ith LR image of the cth channel. Note that we allow for some values of observed LR voxels to be assumed missing (*i.e.*, Not a Number), which enables these values to be filled in during model fitting. Prior to super-resolving a set of MRIs we perform a rigid registration of the observed data to a common reference using the `spm_coreg` routine of SPM12[5].

We cast estimating the HR images ($\mathbf{Y}$), given a set of observed LR images ($\boldsymbol{\mathcal{X}}$), as MAP estimation in the joint probability distribution defined by equation (1):

$$\begin{aligned} & p(\mathbf{Y} \mid \boldsymbol{\mathcal{X}}) = p(\boldsymbol{\mathcal{X}} \mid \mathbf{Y})\; p(\mathbf{Y}) \;/\; p(\boldsymbol{\mathcal{X}}) \\ \Rightarrow \quad & \operatorname*{argmin}_{\mathbf{Y}} \{-\ln p(\mathbf{Y} \mid \boldsymbol{\mathcal{X}})\} \\ \Rightarrow \quad & \operatorname*{argmin}_{\mathbf{Y}} \{-\ln p(\boldsymbol{\mathcal{X}} \mid \mathbf{Y})\; p(\mathbf{Y})\}\,. \end{aligned} \tag{2}$$

For the model to generalise, we estimate its parameters from either the observed data (likelihood and prior hyperparameters) or set them in a general and consistent way (projection matrices). A graphical representation of the generative model is shown in Figure 2. As in practice, there is rarely more than one observation of the same channel, we will from now on drop the summations over i and assume only one observation of each channel. All derivations stay the same, except for additional summations over conditional distributions of LR images. The individual components of our generative model will be further explained in the next three sections.

3.1.1. Model Likelihood

The likelihood function should describe the data generating process of LR images ($\mathbf{x}_c$) from unknown HR images. Its main component is a deterministic projection matrix ($\mathbf{A}_c$) that encodes the slice-selection parameters (orientation, thickness, gap, profile) of an LR image. It is a linear operator that, when applied to the corresponding HR image, creates a noiseless LR version. The second component of the generative process encodes acquisition noise. As MR images are usually reconstructed as the magnitude of an image that was originally complex – and Gaussian noise on complex data gives a Rice distribution in the magnitude image – a Rician noise model would be suitable[6] (Aja-Fernández and Tristán-Vega, 2013). However, it has been shown that the mathematically more tractable Gaussian distribution closely approximates the true Rician noise distribution in MRI (Gudbjartsson and Patz, 1995). We therefore assume the following forward model:

$$\mathbf{x}_c = \mathbf{A}_c \mathbf{y}_c + \epsilon, \qquad \epsilon \sim \mathcal{N}\left(0, \tau_c^{-1}\right), \tag{3}$$

so that the conditional distribution of an observed LR image, given an unknown HR image, is a multivariate Gaussian distribution:

$$\begin{aligned} p(\mathbf{x}_c \mid \mathbf{y}_c) &= \mathcal{N}\left(\mathbf{x}_c \mid \mathbf{A}_c \mathbf{y}_c, \tau_c^{-1} \mathbf{I}\right) \\ &= \frac{\tau_c^{N_c/2}}{(2\pi)^{N_c/2}} \exp\left(-\frac{\tau_c}{2} \left\|\mathbf{x}_c - \mathbf{A}_c \mathbf{y}_c\right\|_2^2\right), \end{aligned} \tag{4}$$

[5] A more elegant way of doing this would be to include registration inside the generative model, such that fitting the model would optimise also some registration parameters (see Discussion).

[6] Note that multi-coil MR images generally do not have Rician noise because of the way the images are reconstructed. The Rician assumption is therefore good for older MR scanners, but becomes a bit of an approximation for more modern systems.

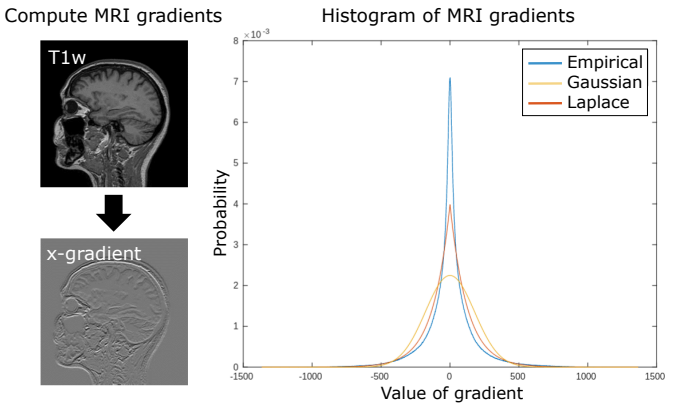

Figure 3: Empirical investigation of the distribution of MR image gradients. By computing the x-, y- and z-gradients of a MR image, and fitting a Gaussian (yellow) and a Laplace distribution (red) to the histogram of these gradients (blue), it can be seen that the Laplace distribution more accurately captures the empirical distribution of MR image gradients.

where τ_c is the precision of the noise of LR image c and $\mathbf{A}_c \in \mathbb{R}^{N_c \times N}$ is the linear operator mapping from HR to LR space. Dropping all terms that do not depend on $\mathbf{y}_c$, the negative log-likelihood can be written as:

$$-\ln p(\mathbf{x}_c \mid \mathbf{y}_c) = \frac{\tau_c}{2} \left\| \mathbf{x}_c - \mathbf{A}_c \mathbf{y}_c \right\|_2^2 + \text{const.} \tag{5}$$

The multivariate Gaussian distribution in equation (4) is a likelihood function that is already well-established in the super-resolution literature (Greenspan et al., 2001; Poot et al., 2010; Shilling et al., 2009).

3.1.2. Model Prior

The prior probability should encode our belief about the unknown HR images ($\mathbf{Y}$). Many types of priors have been devised for image reconstruction problems. The most popular alternative is perhaps the Tikhonov (or ℓ_2 prior), that penalises the squared norm of some image features:

$$p(\mathbf{y}_c) = \mathcal{N}\left(\mathbf{y}_c \mid \mathbf{0}, (\lambda_c \mathbf{L})^{-1}\right), \tag{6}$$

where λ_c is a channel specific regularisation parameter and the precision matrix ($\mathbf{L}$) is designed as to induce correlations between image voxels. This type of prior probability favours images that are smooth when the precision matrix encodes some differential operator $\mathbf{L} = \mathbf{D}^{\mathrm{T}} \mathbf{D}$, so that:

$$-\ln p(\mathbf{y}_c) = \frac{\lambda}{2} \left\| \mathbf{D} \mathbf{y}_c \right\|_2^2 + \text{const.} \tag{7}$$

If the differential operator encodes a first-order derivative, then the negative log-likelihood of this prior is known as a first-order Tikhonov regulariser. The differential operator is in dimension $\mathbf{D} \in \mathbb{R}^{NG \times N}$, where G are the number of differential features.

The underlying assumption of the Tikhonov prior is that the gradients in the HR image have a Gaussian distribution. However, by studying the empirical gradient distribution of a high-resolution, noise-free MR image we see that a Laplace distribution is more suitable (see Figure 3). Discarding terms that do not depend on $\mathbf{y}_c$, this gives the following prior distribution:

$$p(\mathbf{y}_c) \propto \prod_{n=1}^{N} \exp\left(-\lambda_c \left\| \mathbf{D}_n \mathbf{y}_c \right\|_2\right), \tag{8}$$

$$-\ln p(\mathbf{y}_c) = \lambda_c \sum_{n=1}^{N} \left\| \mathbf{D}_n \mathbf{y}_c \right\|_2 + \text{const.} \tag{9}$$

where λ_c is the inverse of the scale parameter of the Laplace distribution, and the operator $\mathbf{D}_n \in \mathbb{R}^{G \times N}$ returns the gradients at the nth data point of $\mathbf{y}_c$. The log of the Laplace distribution in equation (9) is known as (isotropic) total variation (TV) and is another popular method for regularising image reconstruction problems (Rudin et al., 1992). Rather than favouring smooth reconstructions, TV retains edges and therefore leads to less blurry results. Here, to avoid biasing the reconstruction, we extract both the forward and backward first-order finite differences along each dimension, giving $G = 6$ in 3D.

If we assume that the unknown HR images follow the distribution in equation (8), then we do not have any dependencies between channels. Clearly this assumption is false for MR images of the same subject, where most edges should be shared between channels. We therefore propose using the multi-channel total variation (MTV) functional (Sapiro and Ringach, 1996) as our prior probability:

$$p(\mathbf{Y}) \propto \prod_{n=1}^{N} \exp\left(-\sqrt{\sum_{c=1}^{C} \left\| \lambda_c \mathbf{D}_n \mathbf{y}_c \right\|_2^2}\right), \tag{10}$$

$$-\ln p(\mathbf{Y}) = \sum_{n=1}^{N} \sqrt{\sum_{c=1}^{C} \left\| \lambda_c \mathbf{D}_n \mathbf{y}_c \right\|_2^2} + \text{const.} \tag{11}$$

The summation over channels (C) inside of the square root ensures that the channels are 'mixed', making the assumption that the MR images have large smooth regions and a few sharp edges, in similar places. Note that TV is a special case of MTV, when $C = 1$.

3.1.3. Model Parameters

Defining the generative model has given us a set of parameters: the projection matrices ($\mathbf{A}$), noise precisions (τ) and prior parameters (λ). These parameters are all image-specific and it is critical that we set these parameters in a principled way for our model to generalise – it is not feasible to expect users to do manual tuning. This section gives more detail about how the model parameters were chosen.

Projection matrices: The projection matrix ($\mathbf{A}_c$) is a linear mapping from HR to LR image space. It should reproduce the slice-selection process of the MRI scanner. In this work we design the projection matrix as three linear operators, applied in succession as:

$$\mathbf{A}_c = \mathbf{R}_c \mathbf{S}_c \mathbf{T}_c. \tag{12}$$

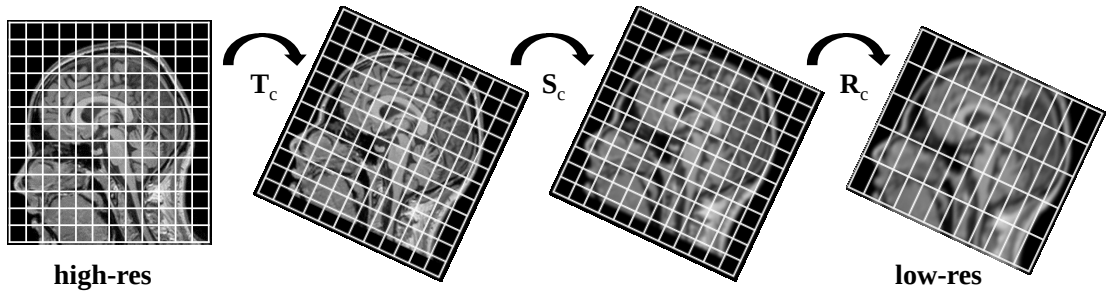

Figure 4: Illustration of the super-resolution forward model ($\mathbf{A}_c$). The operator $\mathbf{T}_c$ resamples from the HR image's FOV to the LR image's FOV, keeping the voxel size of the HR image. The operator $\mathbf{S}_c$ simulates the slice profile of the MRI acquisition. The operator $\mathbf{R}_c$ performs the down-sampling operation from HR to LR space.

The operator $\mathbf{T}_c$ resamples from the HR image's field of view (FOV) to the LR image's FOV, but keeping the voxel size of the HR image. If the slice orientation is at an angle with respect to the HR grid, the corresponding rotation is accounted for. Furthermore, to improve numerical properties of the projection operator, we slightly increase the FOV of the resampled image, which is then adjusted for in the $\mathbf{R}_c$ operator.

The operator $\mathbf{S}_c$ should simulate the slice profile of the MRI acquisition. The slice profile depends on the shape of the radio-frequency (RF) pulse applied during slice selection. This RF pulse can vary a lot from one sequence to the next. Therefore, there is not a single slice profile that suits all acquisitions (Liu et al., 2002). Here, we make the assumption that the slice profile is Gaussian[7]. Applying the $\mathbf{T}_c$ operator before the Gaussian convolution ensures that the kernel is applied in the correct directions. We set the full width at half maximum (FWHM) of the Gaussian kernel to zero in the in-plane directions and to the width of the thick-slice in the thick-slice direction. We additionally modulate the thick-slice direction FWHM by subtracting a slice gap. We computed an estimate of this slice-gap from 29,026 patients MRIs[8]. The estimate we obtain for the slice gap is one third of the width of the slice thickness. This information could be read from the DICOM header of the images. But as our tool works on NIfTI data, this information may not be present, as it can be lost during DICOM-to-NIfTI conversion. The slice gap can however be provided, when available.

The operator $\mathbf{R}_c$ performs the down-sampling operation from HR to LR space. The process of applying $\mathbf{A}_c$ to a HR image is illustrated in Figure 4.

Noise precision: MR scans are usually reconstructed as the magnitude of an image that was originally complex. The Gaussian noise model in equation (3) is therefore just an approximation to a Rician noise model. Hence, we want to estimate the amount of Rician noise in each observed LR image (τ_c). We do so by fitting a mixture of two Rician distributions to the intensity histogram of each MR scan (Ashburner and Ridgway, 2013). We then calculate the precision of the image noise (τ_c) from the class with the smallest noncentrality parameter, which should correspond to air. An example fit is shown in Figure 5a.

Regularisation parameters: Each unknown HR image has a corresponding Regularisation parameter (λ_c). First, note that that gradient values are, in general, correlated with intensity values; the regularisation parameter should therefore be set with respect to the mean intensity in a channel. We observed empirically a linear relationship between the standard deviation of gradient magnitudes σ_c and the mean tissue intensity of an image μ_c. We computed the mean tissue intensity of 1,728 scans from the IXI dataset by fitting a two-class Rician distribution and taking the noncentrality parameter of its non-air component, and regressed the standard deviation of the first-order gradients against it. We obtained the value $k_\lambda = \sigma/\mu = 4.67$; the fit is shown in Figure 5b. Since the variance of a Laplace distribution relates to the scale parameter through the relation $\sigma^2 = 2/\lambda^2$, we can set the parameter λ_c according to:

$$\lambda_c = \frac{\sqrt{2}}{\sigma_c} = \frac{\sqrt{2}}{k_\lambda \mu_c}. \tag{13}$$

[7]Our implementation of the projection matrix however, gives a user the option to easily change the slice profile assumption by simply changing the convolution kernel.

[8]From the DICOM representation of a MR image, whose header contain both the field `Spacing Between Slices` (0018, 0088) and `Slice Thickness` (0018, 0050), the slice gap can be computed as the `Spacing Between Slices` minus the `Slice Thickness`.

3.2. Model Optimisation

With all the individual components of the model defined, the negative log posterior probability can be written

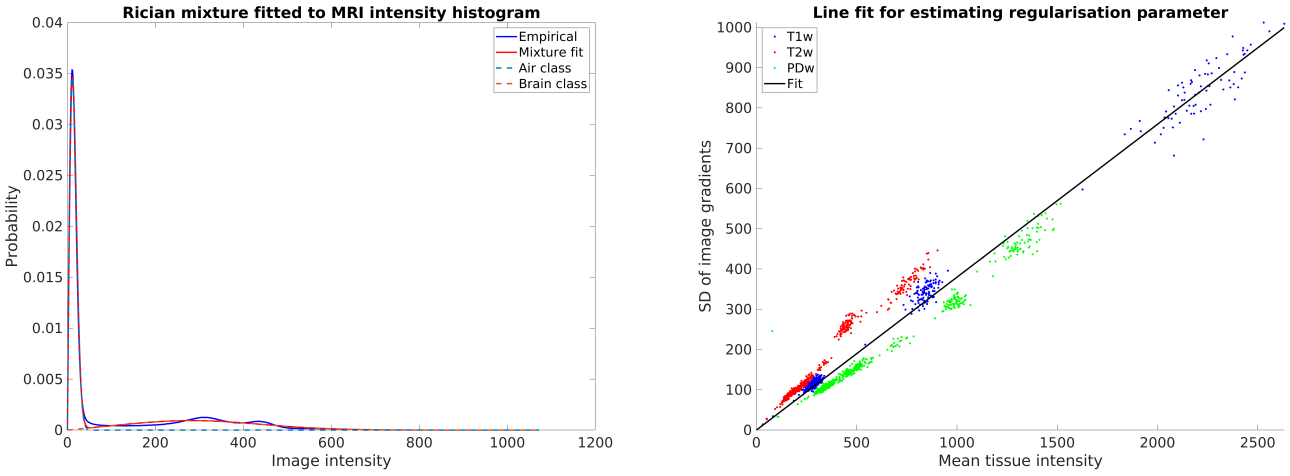

(a) **(b)**

Figure 5: Estimating model parameters for the super-resolution model. (a) A two-class Rician mixture model was fit to the intensity histogram of each MR image. The image noise was computed as the variance of the air class. Note that image intensities in MRI are non-quantitative. (b) A straight line was fit between the mean tissue intensities and the standard deviations of image gradients, computed from the IXI dataset; its coefficient gives us the value of the parameter k_λ.

as:

$$
\begin{aligned}
-\ln\left(p(\boldsymbol{\mathcal{X}} \mid \mathbf{Y})\ p(\mathbf{Y})\right) = &\sum_{c=1}^{C} \frac{\tau_c}{2} \left\|\mathbf{x}_c - \mathbf{A}_c\mathbf{y}_c\right\|_2^2 \\
&+ \sum_{n=1}^{N} \sqrt{\sum_{c=1}^{C} \left\|\lambda_c \mathbf{D}_n \mathbf{y}_c\right\|_2^2} \\
&+ \text{const}, \qquad (14)
\end{aligned}
$$

where the first term on the right-hand side is known as the data term and the second term as the penalty term. The expression in equation (14) is what we want to minimise to obtain the C super-resolved images:

$$
\underset{\mathbf{Y}}{\operatorname{argmin}} \left\{-\ln p(\boldsymbol{\mathcal{X}} \mid \mathbf{Y})\ p(\mathbf{Y})\right\}. \qquad (15)
$$

This optimisation problem is hard to solve because the MTV penalty term is non-differentiable (nonsmooth). It is, however, convex with a global optimum.

A change of variables allows the unconstrained minimisation problem in equation (15) to be rewritten as a constrained minimisation:

$$
\begin{aligned}
\min_{\mathbf{Y}} \quad & \sum_{c=1}^{C} \frac{\tau_c}{2} \left\|\mathbf{x}_c - \mathbf{A}_c\mathbf{y}_c\right\|_2^2 + \sum_{n=1}^{N} \sqrt{\sum_{c=1}^{C} \left\|\mathbf{z}_{nc}\right\|_2^2} \qquad (16) \\
\text{s.t.} \quad & \lambda_c \mathbf{D}_n \mathbf{y}_c = \mathbf{z}_{nc}, \quad \text{for all } n \text{ and } c,
\end{aligned}
$$

where the smooth data term and the nonsmooth penalty term have been decoupled. The constrained form of equation (15) can now be solved efficiently by an algorithm known as alternating direction method of multipliers (ADMM).

3.2.1. Alternating Direction Method of Multipliers

ADMM is part of a class of optimisation methods called proximal algorithms (Boyd et al., 2011). In short, an augmented Lagrangian is formulated from a constrained minimisation problem. This Lagrangian is then minimised in an alternating fashion until a convergence criterion is met. Many methods exist for solving TV problems. We chose an ADMM algorithm because it is straightforward to implement and suitable for the type of optimisation problem in equation (15).

Deriving the general form of the ADMM algorithm starts with an unconstrained minimisation problem:

$$
\min_{\mathbf{y}} \quad \text{data}(\mathbf{y}) + \text{penalty}(\mathbf{y}), \qquad (17)
$$

which is equivalent to the constrained problem:

$$
\begin{aligned}
\min_{\mathbf{y},\mathbf{z}} \quad & \text{data}(\mathbf{y}) + \text{penalty}(\mathbf{z}) \qquad (18) \\
\text{s.t.} \quad & \mathbf{F}_d\mathbf{y} + \mathbf{F}_p\mathbf{z} = \mathbf{d},
\end{aligned}
$$

with constraints defined by $\mathbf{F}_d$, $\mathbf{F}_p$ and $\mathbf{d}$. Note how the optimisation problem in equation (18) has the same form as the super-resolution minimisation in equation (16).

From equation (18), the augmented Lagrangian can be formulated as:

$$
\begin{aligned}
\mathcal{L}_\rho(\mathbf{y}, \mathbf{z}, \mathbf{w}) = &\ \text{data}(\mathbf{y}) + \text{penalty}(\mathbf{z}) \\
&+ \mathbf{w}^{\mathrm{T}}(\mathbf{F}_d\mathbf{y} + \mathbf{F}_p\mathbf{z} - \mathbf{d}) \\
&+ \frac{\rho}{2} \left\|\mathbf{F}_d\mathbf{y} + \mathbf{F}_p\mathbf{z} - \mathbf{d}\right\|_2^2, \qquad (19)
\end{aligned}
$$

where $\mathbf{w} \in \mathbb{R}^P$ holds the Lagrange multipliers and $\rho > 0$ is a descent step-size. From the augmented Lagrangian in

equation (19), the ADMM updates are given as:

$$\mathbf{y}^{k+1} \coloneqq \underset{\mathbf{y}}{\operatorname{argmin}}\, \mathcal{L}_\rho(\mathbf{y}, \mathbf{z}^k, \mathbf{w}^k), \tag{20}$$

$$\mathbf{z}^{k+1} \coloneqq \underset{\mathbf{z}}{\operatorname{argmin}}\, \mathcal{L}_\rho(\mathbf{y}^{k+1}, \mathbf{z}, \mathbf{w}^k), \tag{21}$$

$$\mathbf{w}^{k+1} \coloneqq \mathbf{w}^k + \rho \cdot (\mathbf{F}_d \mathbf{y}^{k+1} + \mathbf{F}_p \mathbf{z}^{k+1} - \mathbf{d}), \tag{22}$$

where equation (20) and equation (21) are known as the proximal operators at parameter ρ for the data and penalty term, respectively. These ADMM updates are usually iterated until some convergence criteria is fulfilled.

3.2.2. ADMM updates for the super-resolution model

In this section we derive the ADMM updates for our super-resolution model. We will work with two tensors $\boldsymbol{\mathcal{Z}}$ and $\boldsymbol{\mathcal{W}}$, which are both of dimensions $N \times C \times G$. We extract column vectors from these tensors, where the subscript of a vector indicates its length: $\mathbf{z}_n = \operatorname{vec}(\boldsymbol{\mathcal{Z}}[n, :, :])$, $\mathbf{z}_c = \operatorname{vec}(\boldsymbol{\mathcal{Z}}[:, c, :])$, $\mathbf{z}_{nc} = \operatorname{vec}(\boldsymbol{\mathcal{Z}}[n, c, :])$, $\mathbf{w}_n = \operatorname{vec}(\boldsymbol{\mathcal{W}}[n, :, :])$ and $\mathbf{w}_c = \operatorname{vec}(\boldsymbol{\mathcal{W}}[:, c, :])$. With the notations introduced we formulate the augmented Lagrangian in equation (19) from equation (16) as:

$$\begin{aligned}\mathcal{L}_\rho(\mathbf{Y}, \boldsymbol{\mathcal{Z}}, \boldsymbol{\mathcal{W}}) =& \sum_{c=1}^{C} \frac{\tau_c}{2} \left\|\mathbf{x}_c - \mathbf{A}_c \mathbf{y}_c\right\|_2^2 + \sum_{n=1}^{N} \left\|\mathbf{z}_n\right\|_2 \\ &+ \sum_{c=1}^{C} \mathbf{w}_c{}^{\mathrm{T}} (\lambda_c \mathbf{D} \mathbf{y}_c - \mathbf{z}_c) \\ &+ \frac{\rho}{2} \sum_{c=1}^{C} \left\|\lambda_c \mathbf{D} \mathbf{y}_c - \mathbf{z}_c\right\|_2^2, \end{aligned} \tag{23}$$

where we have made use of the fact that, for a fixed n:

$$\sqrt{\sum_c \left\|\mathbf{z}_{nc}\right\|_2^2} = \sqrt{\sum_c \sum_g (z_{ncg})^2} = \left\|\mathbf{z}_n\right\|_2. \tag{24}$$

From the augmented Lagrangian in equation (23) the ADMM updates can be derived as:

$$\begin{aligned}\mathbf{y}_c^{k+1} \coloneqq \underset{\mathbf{y}_c}{\operatorname{argmin}} \Big(& \frac{\tau_c}{2} \left\|\mathbf{x}_c - \mathbf{A}_c \mathbf{y}_c\right\|_2^2 + \lambda_c \mathbf{w}_c^{k\,\mathrm{T}} \mathbf{D} \mathbf{y}_c \\ & + \frac{\rho}{2} \left\|\lambda_c \mathbf{D} \mathbf{y}_c - \mathbf{z}_c^k\right\|_2^2 \Big), \end{aligned} \tag{25}$$

$$\begin{aligned}\mathbf{z}_n^{k+1} \coloneqq \underset{\mathbf{z}_n}{\operatorname{argmin}} \Big(& \left\|\mathbf{z}_n\right\|_2 - \mathbf{w}_n^{k\,\mathrm{T}} \mathbf{z}_n \\ & + \frac{\rho}{2} \left\|\lambda_c \mathbf{D}_n \mathbf{y}_c^{k+1} - \mathbf{z}_n\right\|_2^2 \Big). \end{aligned} \tag{26}$$

The updates in equation (25) and equation (26) give C optimisation problems for the HR images $\mathbf{Y}$ and N optimisation problems for the variables $\boldsymbol{\mathcal{Z}}$. From equation (22) the estimate of the Lagrange multiplier is:

$$\mathbf{w}_c^{k+1} \coloneqq \mathbf{w}_c^k + \rho \cdot (\lambda_c \mathbf{D} \mathbf{y}_c^{k+1} - \mathbf{z}_c^{k+1}), \quad \text{for all } c. \tag{27}$$

ADMM update for $\mathbf{Y}$:. The optimisation problem in equation (25) is simply regularised least-squares with a closed-form solution given by:

$$\begin{aligned}\mathbf{y}_c^{k+1} =& \Big(\tau_c \mathbf{A}_c{}^{\mathrm{T}} \mathbf{A}_c + \rho \lambda_c^2 \mathbf{D}^{\mathrm{T}} \mathbf{D} \Big)^{-1} \\ & \Big(\tau_c \mathbf{A}_c{}^{\mathrm{T}} \mathbf{x}_c - \lambda_c \mathbf{D}^{\mathrm{T}} (\mathbf{w}_c - \rho \mathbf{z}_c) \Big). \end{aligned} \tag{28}$$

This system is too large to be inverted directly, and a conjugate gradient method is often used as an alternative (Hestenes and Stiefel, 1952). Here, for increased speed and convergence, we instead use a Newton's method. Writing the objective function as:

$$\begin{aligned}\mathcal{L}(\mathbf{y}_c) =& \frac{\tau_c}{2} \left\|\mathbf{x}_c - \mathbf{A}_c \mathbf{y}_c\right\|_2^2 + \lambda_c \mathbf{w}_c{}^{\mathrm{T}} \mathbf{D} \mathbf{y}_c \\ & + \frac{\rho}{2} \left\|\lambda_c \mathbf{D} \mathbf{y}_c - \mathbf{z}_c\right\|_2^2, \end{aligned} \tag{29}$$

we get its gradient as:

$$\begin{aligned}\frac{\partial \mathcal{L}(\mathbf{y}_c)}{\partial \mathbf{y}_c} =& (\tau_c \mathbf{A}_c{}^{\mathrm{T}} \mathbf{A}_c + \rho \lambda_c^2 \mathbf{D}^{\mathrm{T}} \mathbf{D}) \mathbf{y}_c \\ & + \lambda_c \mathbf{D}^{\mathrm{T}} (\mathbf{w}_c - \rho \mathbf{z}_c) - \tau_c \mathbf{A}_c{}^{\mathrm{T}} \mathbf{x}_c, \end{aligned} \tag{30}$$

and Hessian as:

$$\frac{\partial^2 \mathcal{L}(\mathbf{y}_c)}{\partial \mathbf{y}_c \partial \mathbf{y}_c{}^{\mathrm{T}}} = (\tau_c \mathbf{A}_c{}^{\mathrm{T}} \mathbf{A}_c + \rho \lambda_c^2 \mathbf{D}^{\mathrm{T}} \mathbf{D}). \tag{31}$$

Since the problem is quadratic, Newton's method would solve it in one step, which is equivalent to computing the closed-form solution in equation (28). However, obtaining the full Hessian is computationally difficult. We therefore replace the true Hessian by a majorising matrix:

$$\mathbf{H}_c = \operatorname{diag}(\tau_c \mathbf{A}_c{}^{\mathrm{T}} \mathbf{A}_c \mathbb{1}) + \rho \lambda_c^2 \mathbf{D}^{\mathrm{T}} \mathbf{D}, \tag{32}$$

where $\mathbb{1} \in \mathbb{R}^N$ is a vector of ones. This approximation, which can be inverted in linear time using a multigrid method (Ashburner, 2007), is more positive-definite than the true Hessian in the Loewner ordering sense (see Lemma S.3 in Chun and Fessler (2017)) and therefore ensures convergence. This gives us the following update step:

$$\mathbf{y}_c^{k+1} = \mathbf{y}_c - \mathbf{H}_c^{-1} \frac{\partial \mathcal{L}(\mathbf{y}_c)}{\partial \mathbf{y}_c}. \tag{33}$$

ADMM update for $\boldsymbol{\mathcal{Z}}$:. By some algebraic manipulations we can rewrite equation (26) in the equivalent form:

$$\begin{aligned}\mathbf{z}_n^{k+1} = \underset{\mathbf{z}_n}{\operatorname{argmin}} \Big(& \frac{\rho}{2} \left\| \mathbf{z}_n - \left(\frac{1}{\rho} \mathbf{w}_n + \lambda_c \mathbf{D}_n \mathbf{y}_c \right) \right\|_2^2 \\ & + \left\|\mathbf{z}_n\right\|_2 + \text{const} \Big), \end{aligned} \tag{34}$$

where the constant contains terms that do not depend on $\mathbf{z}_n$. This gives us an optimisation problem with an ℓ_2 data

Algorithm 1 Multimodal super-resolution

Coregister input images ($\mathbf{X}$).
Estimate model parameters ($\boldsymbol{\tau}, \boldsymbol{\lambda}$).
Initialise variables to zero ($\mathbf{Y}, \boldsymbol{\mathcal{Z}}, \boldsymbol{\mathcal{W}}$).
while not coverged **do**
  for $c = \{1, \ldots, C\}$ **do**
    # Loop over channels (distributed)
    Compute $\mathbf{y}_c^{k+1}$ by equation (33), when given $\mathbf{z}_c^k$ and $\mathbf{w}_c^k$.
  end for
  for $n = \{1, \ldots, N\}$ **do**
    # Loop over HR voxels
    Compute $\mathbf{z}_n^{k+1}$ by equation (37), when given $\mathbf{y}_n^{k+1}$ and $\mathbf{w}_n^k$.
  end for
  for $c = \{1, \ldots, C\}$ **do**
    # Loop over channels
    Compute $\mathbf{w}_c^{k+1}$ by equation (22), when given $\mathbf{y}_c^{k+1}$ and $\mathbf{z}_c^{k+1}$.
  end for
end while

term and an ℓ_1 penalty term. A more general formulation of this problem is:

$$\underset{\mathbf{s}}{\operatorname{argmin}} \left(\frac{\beta}{2} \left\| \mathbf{s} - \mathbf{t} \right\|_2^2 + \alpha \left\| \mathbf{s} \right\|_2 \right), \tag{35}$$

which has a closed-form solution given by (proof given in, *e.g.*, Yang et al. (2009)):

$$\mathbf{s}(\mathbf{t}) = \max\left\{ \left\| \mathbf{t} \right\|_2 - \frac{\alpha}{\beta}, 0 \right\} \odot \frac{\mathbf{t}}{\left\| \mathbf{t} \right\|_2}, \tag{36}$$

where $\odot$ denotes the Hadamard product. The solution to the optimisation problem in equation (34) is therefore given by:

$$\mathbf{z}_n^{k+1} = \max\left\{ \left\| \frac{1}{\rho}\mathbf{w}_n + \lambda_c \mathbf{D}_n \mathbf{y}_c \right\|_2 - \frac{1}{\rho}, 0 \right\} \odot \frac{\frac{1}{\rho}\mathbf{w}_n + \lambda_c \mathbf{D}_n \mathbf{y}_c}{\left\| \frac{1}{\rho}\mathbf{w}_n + \lambda_c \mathbf{D}_n \mathbf{y}_c \right\|_2}. \tag{37}$$

3.3. Implementation Details

Algorithm 1 shows the steps for super-resolving a set of thick-sliced patient scans with the proposed model. The process is computationally intensive and we take care to provide an efficient implementation. The software is written in a mixture of MATLAB and C code. There are large memory requirements, which are likely to exceed the random-access memory (RAM) of some workstations. To save memory, all the computations are therefore performed using single precision floating point. This lower precision has negligible effect on the numerical stability. We solve for $\mathbf{Y}$ efficiently using a multigrid technique (Ashburner, 2007). The Newton update can be iterated over to get a closer fit to the solution. In this work, however, a single update is used to reduce computational time. Furthermore, the loop solving for each $\mathbf{Y}$ is distributed, so that a separate process handles each iteration. Finding the optimal step-size ρ is an open-problem (Dohmatob et al., 2014), and though under mild conditions ADMM converges for any value of ρ, the convergence rate depends on ρ. Here, we use the heuristic:

$$\rho = \frac{\sqrt{\operatorname{mean}(\{\lambda_c\}_{c=1}^C)}}{\operatorname{mean}(\{\tau_c\}_{c=1}^C)}, \tag{38}$$

which we observe empirically gives good convergence properties. Furthermore, algorithm convergence is defined by the relative change in objective value: $2 \cdot (l^k - l^{k+1})/(l^k + l^{k+1})$, being less than 10^{-4}. The objective value (l) is computed from equation (14). Finally, we define the HR images' FOV as the bounding box that contains all LR images' FOV, and we set the voxel size of the HR images to 1 mm isotropic.

4. Evaluation

The aim of this section is to assess the effectiveness of the MTV prior, compared with classically used regularisers for super-resolving multi-contrast MR datasets, and to illustrate the proposed model's ability to process a large clinical dataset.

4.1. High-resolution IXI dataset

The IXI dataset[9] contains multimodal MR volumes, with T1w, T2w and PDw images, of 576 healthy subjects, acquired on 1.5T and 3T systems at three different centres. All images have close to 1 mm isotropic resolution. This dataset was used to (1) validate the robustness of the noise variance estimation by adding known amounts of Rician noise and estimating it; (2) compare our heuristic for setting regularisation parameters, with optimal values obtained by grid-search; (3) compare the efficiency of two iterative methods (conjugate gradient and approximate Newton) for solving a quadratic optimisation problem; (4) compare four different methods for super-resolving MRIs: 4th order b-spline (BS) interpolation, first-order Tikhonov (FOT), TV and MTV.

LR images were generated by applying the forward projection operator ($\mathbf{A}$) to HR images, such that LR images had thick slices in one direction. Thick-slice directions were picked randomly, but were always orthogonal across contrasts (*e.g.*, axial for T1w, coronal for T2w, sagittal for PDw). Figure 6 shows an example of simulated LR images from HR images. Comparisons between methods are

[9] `http://brain-development.org/ixi-dataset/`

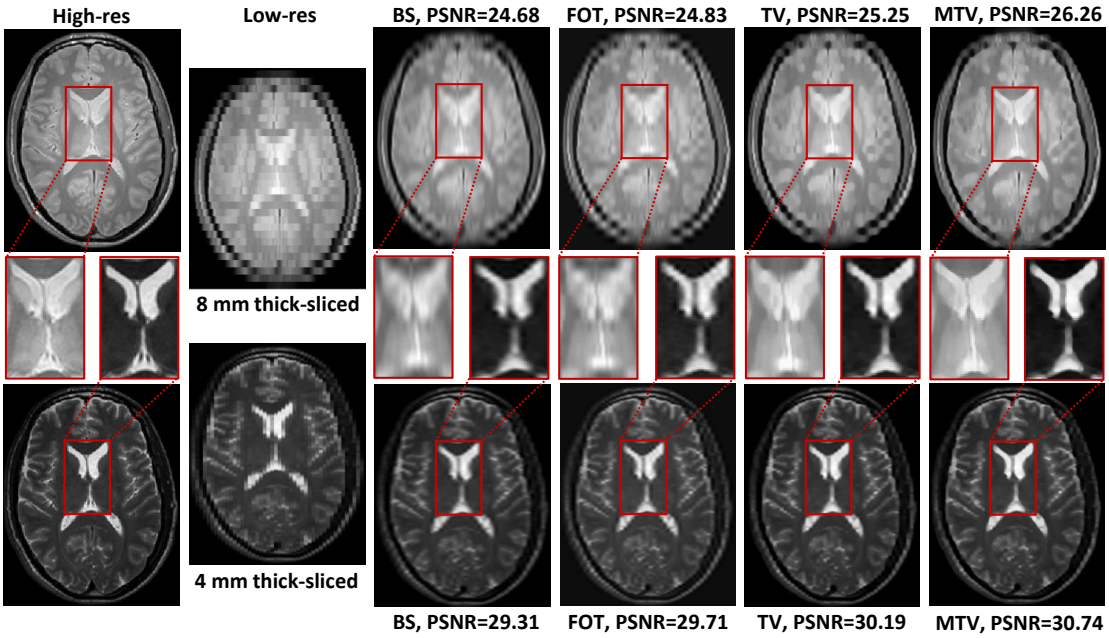

Figure 6: Example of simulating and super-resolving from the IXI dataset. Two LR images were simulated from two HR images (PDw and T2w). The HR images were then reconstructed using four methods: BS, FOT and TV are single-channel SR techniques, capable of combining LR images of only one channel; MTV on the other hand, a multi-channel method, combines information from both channels.

based on the root-mean-square error (RMSE):

$$\mathrm{RMSE} = \sqrt{\sum_{n=1}^{N} \left(y_n^{\mathrm{recon}} - y_n^{\mathrm{ref}}\right)^2}, \tag{39}$$

and the peak signal-to-noise ratio (PSNR):

$$\mathrm{PSNR} = 20 \log_{10} \left(\frac{\max\left(\mathbf{y}^{\mathrm{ref}}\right)}{\mathrm{RMSE}} \right), \tag{40}$$

two widely used metrics for image reconstruction. These metrics were computed for each contrast. We also computed Dice scores between GM and WM segmentations obtained by applying SPM12's unified segmentation (with default parameters) to the super-resolved and HR images. Segmentation is a typical processing task in neuroimaging as it allows for morphometric analyses to be conducted.

FOT, defined in equation (7) and TV, defined in equation (9), were implemented within the same framework as MTV. Therefore, they used the same projection matrices and parameters. B-spline interpolation is not technically a super-resolution technique, but is often used in practice to reslice low-resolution images prior to automated processing. For b-spline interpolation, if multiple LR images of the same contrast are available, they are simply averaged.

Noise Precision: All 1,728 IXI scans were used in this experiment. A known amount of Rician noise, as a percentage of the mean image intensity (1%, 2.5%, 5%, 10%), was added to each image. The two-class Rician mixture model was then fit to the intensity histogram of the noisy images. The variance of the cluster with the lowest noncentrality parameter was used as an estimate of the image noise percentage. Table 1 shows the mean and standard deviation, across subjects, of the estimated noise variance percentage. These results show that the Rician mixture model can accurately estimate a wide range of noise levels. Note that there is already Rician noise present in the images. However, the amount of Rician noise that is added is an order of magnitude greater than the intrinsic noise.

Regularisation Parameter: Four images from different subjects and contrasts (T1w, T2w, PDw and diffusion-weighted (DW)), were used to validate whether the heuristic devised in section 3.1.3 to estimate the prior parameter (λ) yields proper regularisation values. LR images with seven millimetre slice-thickness were generated and a grid-search over the regularisation parameter was performed, (in the range $\left[10^{-4}, 1\right]$, with step size 0.2). For each value, PSNR between the resulting MTV super-resolved images and the known ground-truth was computed. A DW image was included to investigate whether the heuristic generalises to contrasts not part of the training set. The result of each grid-search, with the corresponding heuristic estimates marked by crosses, can be seen in Figure 7. This experiment shows that the method for estimating the regularisation parameter allows near-optimal reconstructions to be produced, even for unseen contrasts.

Approximate Newton Solver: The update-step for $\mathbf{Y}$ entails solving a large linear system, which is often done iteratively using the conjugate gradient method

Table 1: Validating the estimate of the noise precision parameter (for 1,728 subjects). Showing the simulated noise percentages, and the noise percentages estimated by fitting the two class Rician mixture model. Shown as mean±std.

Ground-truth (%)	1	2.5	5	10
Estimated (%)	1.10 ± 0.76	2.54 ± 0.51	5.23 ± 1.01	10.31 ± 2.49

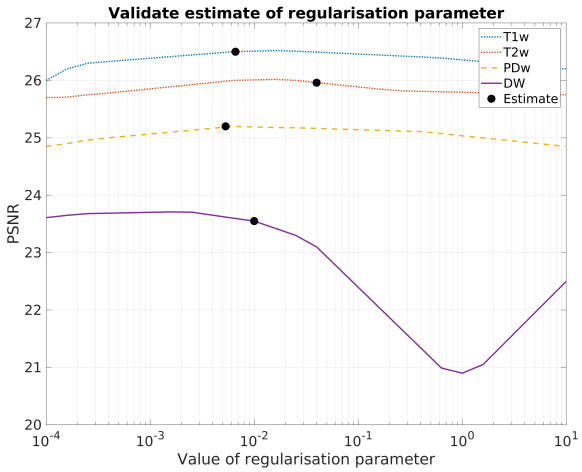

Figure 7: Validation of estimating the regularisation parameter. A grid-search over the regularisation parameter (λ) was performed for four different contrasts, and PSNR between the reconstruction and reference image was computed. The regularisation parameter obtained heuristically is marked by a dot.

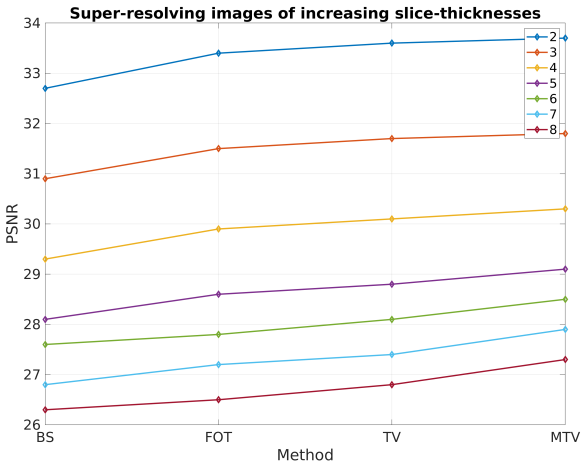

Figure 8: Super-resolving images of different slice-thicknesses (for 20 subjects). As the simulated slice-thickness increases (top to bottom), MTV super-resolution results improve favourably compared with the single-channel methods (BS, FOT, TV).

(Hestenes and Stiefel, 1952). Here, we show that, for this particular problem, an approximate Newton method (based on a majoriser of the full Hessian and solved with a multigrid algorithm) converges faster than the conjugate gradient method. T1w, T2w and PDw image were simulated, with 6 mm slice thicknesses and different thick-slice directions. The MTV super-resolution algorithm was then run, where the update for $\mathbf{Y}$ was solved either using the conjugate gradient or the approximate Newton method. Both solution method were iterated for a fixed number of iterations (50). Figure 9 shows the evolution of the negative log-likelihood over computation time. This total computation time takes into account both the number of iterations and the computation time per iteration. The approximate Newton solver converges faster than the conjugate gradient solver. Note that we did not use pre-conditioning, which may have led to increased conjugate gradient solver performance.

Multi-channel Super-Resolution: All IXI subjects were used to simulate LR images. For each subject, the slice direction and thickness (between two and eight millimetre) were chosen at random. The simulated LR images were super-resolved using BS, FOT, TV and MTV. Among these, only MTV makes joint use of information distributed across contrasts. Example reconstructions obtained with each method can be seen in Figure 6.

For each contrast, PSNR was computed between the reference and super-resolved images. Table 2 shows the average PSNR and MTV obtained the greatest mean and lowest standard deviation. Figure 8 additionally shows average PSNRs for different slice thicknesses, in which MTV once again performs favourably.

Reference and super-resolved images were also segmented into GM and WM and cerebrospinal fluid (CSF) using SPM12, with the reference segmentation considered as ground-truth, and the Dice coefficient was computed. The results can be seen in Table 3 where MTV obtained the highest Dice score.

4.2. Clinical Data

In the previous section we showed that multi-channel super-resolution outperforms some established single-channel techniques, on simulated data. This result is promising as we now move on to evaluating the method on real, clinical-grade MR data – a far more challenging scenario. Conversely to simulated data, there is no ground truth for clinical data. Therefore, we propose to evaluate implicitly the quality of the reconstructed images by using them as input to machine learning models to predict known, noise-free features: age and sex.

The dataset we used consists of 1,046 patient's MRIs, with 615 males and 431 females. The dataset was acquired on a diversity of scanners and clinical indications at UCLH (University College London Hospitals, London, UK) in the

Table 2: Results comparing single- vs multi-channel super-resolution. BS, FOT and TV are all single-channel techniques, MTV is multi-channel. PSNRs are shown as mean±std.

Channel	BS	FOT	TV	MTV
T1w	29.89 ± 9.35	30.51 ± 10.76	30.71 ± 10.84	$\mathbf{31.19 \pm 9.41}$
T2w	28.10 ± 8.02	28.71 ± 8.85	28.98 ± 8.96	$\mathbf{29.58 \pm 7.86}$
PDw	28.37 ± 9.85	28.59 ± 10.02	28.95 ± 9.85	$\mathbf{29.96 \pm 8.93}$

Table 3: Results for segmenting super-resolved images (for 576 subjects). Dice scores for different reconstruction methods were computed for GM, WM and CSF tissue segmentations, using HR segmentations as references. Results shown as mean±sd.

Tissue class	BS	FOT	TV	MTV
GM	0.831 ± 0.001	0.838 ± 0.001	0.842 ± 0.002	$\mathbf{0.887 \pm 0.002}$
WM	0.866 ± 0.001	0.874 ± 0.002	0.878 ± 0.001	$\mathbf{0.891 \pm 0.001}$
CSF	0.842 ± 0.002	0.852 ± 0.001	0.856 ± 0.001	$\mathbf{0.885 \pm 0.002}$

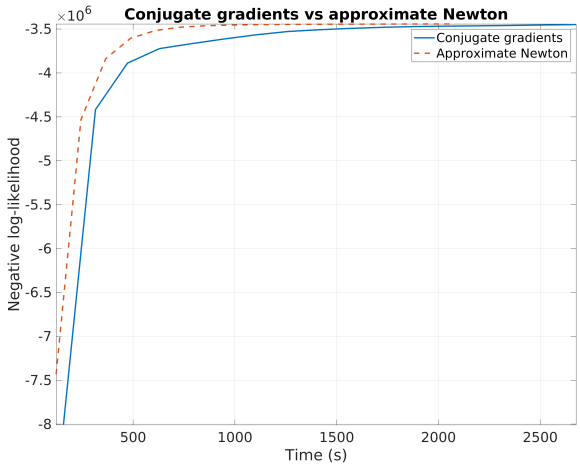

Figure 9: Conjugate gradients vs approximate Newton for solving the super-resolution problem. Time in seconds is plotted against negative log-likelihood. It can be seen that the approximate Newton method has faster convergence.

context of routine clinical care. The dataset comprises three contrasts (T1w, T2w and FLAIR), each with a different thick-slice direction; the average slice-thickness over the whole dataset is 6.5 mm. Commonly, the images have only partial brain coverage in the thick-slice direction, with the outer most slices excluded. The age distribution of the dataset is shown in Figure 12a.

The gist of our validation relies on training machine learning models to predict age and sex from tissue segmentations of patient MR images. It is now well known that these features can be very accurately predicted from brain images (Cole et al., 2017; He et al., 2018; Monté-Rubio et al., 2018; Smith et al., 2019). Here, we follow the procedure of Monté-Rubio et al. (2018). Since (accurate) normalised segmentations capture relevant and important anatomical features of the MRIs, predictive accuracy can be used as a measure of the quality of a super-resolution model.

For each subject in the dataset, the LR images were super-resolved to 1 millimetre isotropic with BS (4th order) or MTV, and segmented using SPM12's unified segmentation routine (Ashburner and Friston, 2005), with default parameters. This routine outputs normalised, non-modulated, GM, WM and Other (1 - GM - WM) maps, that were smoothed with a Gaussian kernel of 12 mm full-width at half-maximum (FWHM). The concatenated smoothed maps were used as a feature vector for machine-learning. Two Gaussian process models were trained, using 10-fold cross-validation, to predict age and sex from this feature vector. The PRoNTo toolbox (Schrouff et al., 2013) was used to make these predictions. Using a convolutional neural network based model could have been an option, but recent studies suggest that kernel methods performs comparably for predictive tasks similar to the ones performed here (He et al., 2018).

The results of both the regression and classification task are shown in Table 4. Age regression results are reported in years using the root mean square error (RMSE), error standard deviation (SD), mean error (bias) and Pearson's correlation coefficient; sex classification accuracy is reported in percentage, and the lower and upper bound over the 10 folds are included. Furthermore, for the MTV case, a scatter plot of the individual predictions for the regressions task is shown in Figure 12b, and a receiver operator curve (ROC) for the classification task is shown in Figure 12c. Images and non-smoothed native space segmentations, for an example patient, are shown in Figure 10. Our results make it quite clear that the segmentations produced from the super-resolved images have more predictive power. This is true for both the regression and classification task (*c.f.* Table 4). In particular for the classification task, where the improvement in accuracy is 3.3 percentage points. It also evident from the example segmentations in Figure 10 that anatomical features are more clearly defined in the super-resolved segmentations. Furthermore, comparing, *e.g.*, the super-resolved close-up of the T1w image with its baseline counterpart, it can be seen that the mismatched fields of views have been filled in for the super-resolution case. Finally, the runtime of the algorithm to super-resolve three LR images, as was performed in this evaluation, is under 30 minutes on a modern workstation. The runtime scales linearly with the number of channels.

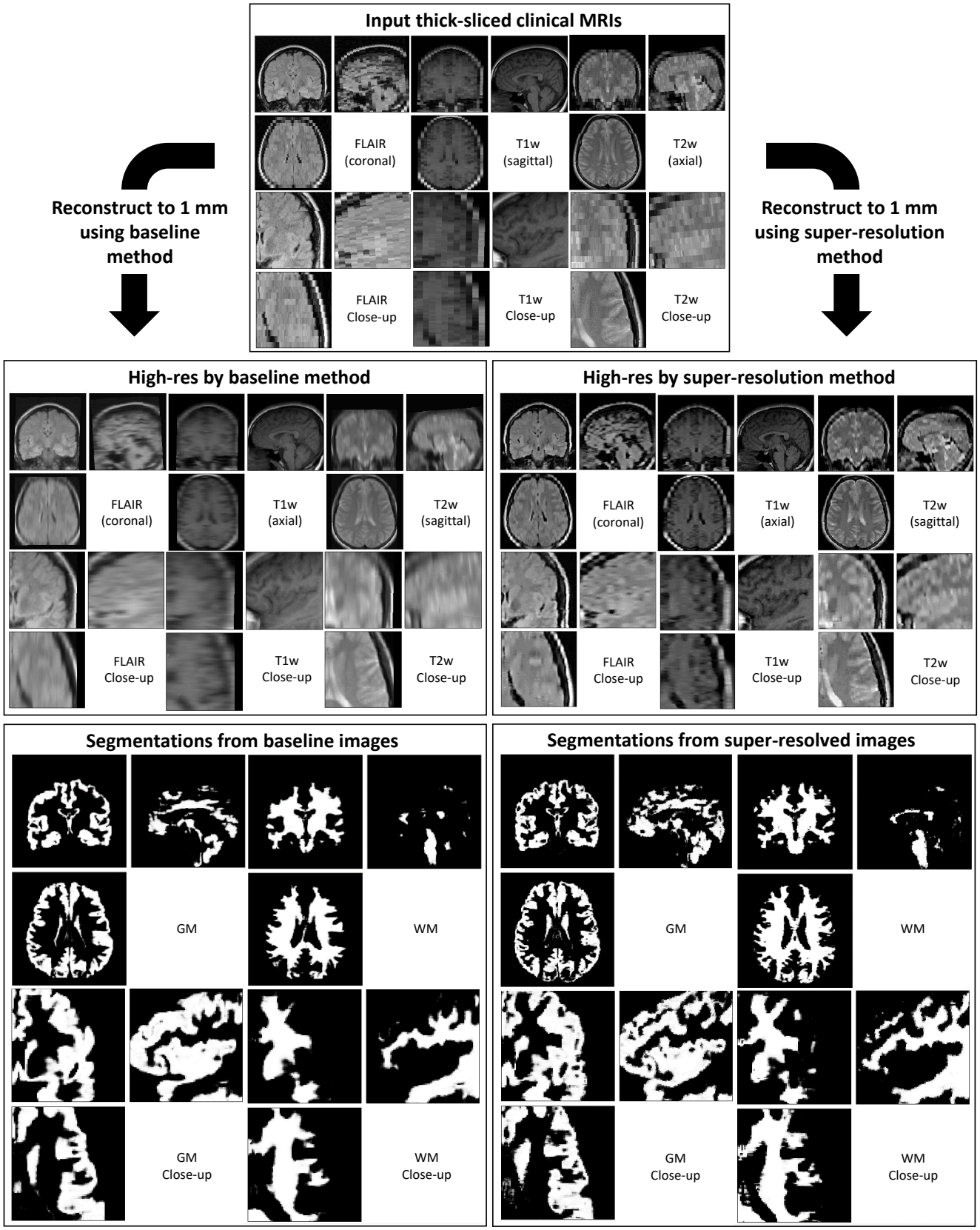

Figure 10: Example results for baseline vs super-resolution, for a randomly selected patient. The box on top shows the three input clinical scans (FLAIR, T1w and T2w). These three scans are reconstructed to 1 mm isotropic voxel size, using either the baseline (left) or the super-resolution method (right). It is clear that the multi-channel segmentation output (GM and WM), produced from the super-resolved images have better anatomical detail. For example, the WM has a clearer delineation close to the cortex.

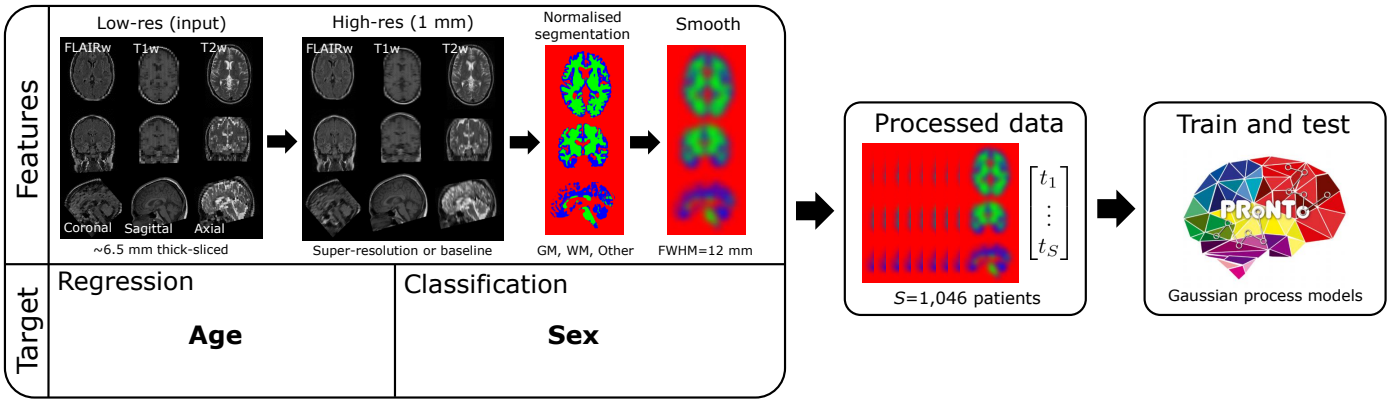

Figure 11: Evaluation of the super-resolution method on clinical data. Feature vectors are obtained by concatenating smoothed, gray matter (GM), white matter (WM) and other segmentations. These segmentations are produced from multi-channel MRIs that has been reconstructed to 1 mm isotropic voxel size using either super-resolution or a baseline method. The prediction targets are either the age or sex of the patients. Predictive performance is then evaluated, for both, methods using Gaussian process models in the PRoNTo toolbox.

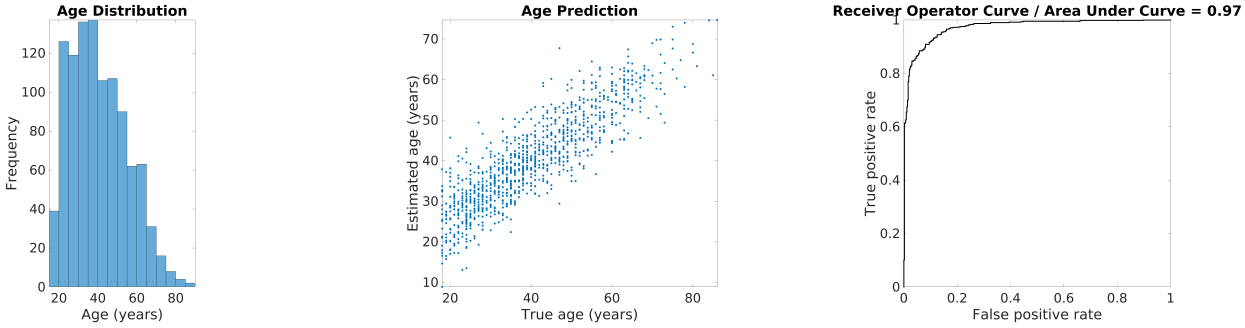

(a) **(b)** **(c)**

Figure 12: Results for evaluating the super-resolution model. (a) Age distribution of the 1,046 patients in the clinical dataset. Mean value is 40.1 and standard deviation is 14.3 years. (b) Scatter plot of the individual predictions for the regressions task. (c) ROC curve for the classification task, where an AUC of 0.97 was obtained.

5. Discussion

This paper presents a super-resolution tool that can be applied to large datasets of clinical MR scans. Commonly in such datasets, each patient has a collection of images acquired with different MR sequences. Currently, when performing some multi-channel analysis, these images are often simply interpolated to the same size. The model proposed here is an alternative to interpolation that better leverages these multiple MR contrasts. The model builds on a principled probabilistic generative model. The novelty of the model lies in the MTV prior, which allows a joint probability distribution across MR contrasts to be modelled. All model parameters are set automatically, and no fine-tuning is necessary, allowing large datasets to be processed with variable slice-thicknesses and MR contrasts. We showed that, when the super-resolution model is used as a preprocessing step, subsequent machine-learning tasks have improved results.

Data-driven models currently show state-of-the art performances in many image processing tasks and could be an alternative to the approach proposed in this paper. However, generalisability is still an issue with many such methods, as they excel in scenarios where the unseen data is close to data the model was trained on but does not extrapolate well on out-of-sample test data. This is because data-driven models construct an empirical prior from the data, which leads to a flexible, highly parametrised model – where minor prior assumptions are necessary – but where overfitting to a training population can be an issue. This is especially risky with pathological imaging, because pathology adds further diversity on already hugely diverse normal biology. Model-based methods, on the other hand, require prior assumptions to be made. To design priors as flexible as ones learnt by data-driven techniques is extremely challenging, and simplified assumptions are therefore often made. If the prior assumption is close to the data generating process, and the forward model and statistical properties of the data is too, then model-based methods can perform well on out-of-sample data (and will not require any retraining). Interestingly, methods have been developed that combine model- and data-driven approaches (Adler and Öktem, 2018; Brudfors et al., 2019; Dalca et al., 2019). This combination would be an in-

Table 4: Results for predicting age and sex from normalised brain segmentations (for 1,046 patients). We compared the proposed super-resolution model to a baseline method, which reslices using 4th order b-spline interpolation. Age regression results are reported in years using the root mean square error (RMSE), error standard deviation (SD), mean error (bias) and Pearson's correlation coefficient. Sex classification accuracy is reported in percentage, where the lower and upper bound over the 10 folds are included.

	Age (years)				Sex (%)		
Method	RMSE	SD	Bias	Correlation	Accuracy	Lower bound	Upper bound
Baseline	6.91	9.89	-1.73	0.85	87.8	85.6	89.6
Super-resolution	6.32	8.66	-1.18	0.88	91.1	89.2	92.7

teresting future direction for the super-resolution model proposed in this paper.

The model we have proposed could be of value in translating methods that have shown good results on research data to clinical imaging. For example, many techniques based on machine (deep) learning show promising results on analysing neuroimaging data (Litjens et al., 2017). However, a model trained on HR data may struggle when given as input LR clinical data. Applying our super-resolution model as a preprocessing step, reconstructing HR versions from the LR input, could facilitate this transition. The evaluation also showed that the tissue segmentation performance of a widely used neuroimaging package improves when the multi-channel input images are super-resolved, compared with simply being interpolated. Furthermore, the model could easily be used for multi-channel denoising by replacing the projection matrix in equation (4) with identity[10].

However, metric scores such as those used in this study are specific to the data that was used to evaluate the model. Any claim that a method generalises to the huge variability present in clinical MR scans should therefore be taken with a pinch of salt. This is not only because the imaging data varies greatly: in image contrast, intra-subject alignment and voxel size; but also because the scanner acquiring the images may not have computed the correct voxel sizes, slice-thicknesses, *etc.* In our evaluation, we used a clinical dataset with a large variability among patient scans. Still, this is no guarantee that our model will work on any clinical MR data. However, data specificity is likely to be greater the more flexible the model is, such that highly parameterised models may suffer more from this specificity.

The model proposed in this paper could be made, possibly, more robust in a few ways. One is related to our assumptions regarding the slice profile and slice gap. These parameters are highly variable and assuming them as fixed, as is currently done, can lead to inexact super-resolved images. Of course, a user could change these parameters themselves if they know their values. However, they sometimes cannot be obtained. A principled solution to this problem would be to extend the parametrisation of the projection matrices to model both slice gap and profile. Although a non-trivial modelling problem, this would allow us to estimate the most likely such parameters. Misalignment between scans could be another explanation for poor super-resolved images, as our edge-based prior distribution is highly dependent on well registered LR images. Rather than performing an initial rigid registration of the LR images (as is currently done) improved alignment could be achieved by modifying the forward model in equation (3) to incorporate a rigid transformation. The optimal parameters could then be found by Gauss-Newton optimisation, similar to what is done in (Ashburner and Ridgway, 2013).

A well known fact is that TV introduces stair-casing effects on flat areas, which are abundant in brain MRI. However, the MTV regularisation proposed in this paper seems not to suffer from such artefacts. This is probably because MTV uses gradients distributed over all contrasts, which often have orthogonal thick-slice directions. Hence, an image area containing flat gradients in one channel may very well have more informative gradients in another channel. Another factor that suppresses these stair-casing artefacts is our parametrisation of the differential operator, which computes the gradient using both the forward and the backward finite differences.

Many different algorithms are available to solve nonsmooth optimisation problems such as the one that arises when using a nonsmooth TV prior. Here, we used an ADMM algorithm because it is relatively fast and easy to implement, and since the quadratic problem that arises can be easily solved with a multigrid solver that assumes a stationary penalty over gradients. However, it makes proper marginalisation of the (latent) HR image difficult. An alternative could be to use an approach based on reweighted least-squares (RLS) (Bach et al., 2012; Daubechies et al., 2010; Grohs and Sprecher, 2016), which makes use of the bound:

$$\|\mathbf{z}\|_2 = \min_{w>0} \left\{ \frac{1}{2w} \|\mathbf{z}\|_2^2 + \frac{w}{2} \right\}. \tag{41}$$

We could substitute this bound, with $\mathbf{z} = \mathbf{D}_n\mathbf{Y}$, in the joint log-distribution. However, this would require extending the multigrid solver to handle non-stationary penalties. Furthermore, instead of looking for a MAP solution, an approximate Gaussian posterior that factorises over voxels and channels could be obtained using variational Bayes (Attias, 2000). When used in combination with RLS, this posterior would be bounded by a Gaussian. Finally, commonalities between channels do not solely reduce to edges; intensities co-vary as well. Mutual information between

[10]Running the denoising version of the model is an option in our software implementation.

channels could be taken into account by introducing an additional, independent, prior over the reconstructed image in the form of a multivariate Gaussian mixture (Brudfors et al., 2019). This would be, in practice, a joint reconstruction and segmentation framework. When multiple images are available, commonalities across subjects could be learnt as well by using a learnable shape and intensity model (Ashburner et al., 2019; Blaiotta et al., 2018). Such an extended Bayesian framework may eventually be able to compete with (deep) learning-based approaches, or could even be defined as to include such models in the generative process (Brudfors et al., 2019).

Clinical Data:

The clinical data that was used in this paper is a sample of anonymized MR studies obtained within the clinical routine, for which ethical and regulatory approval has been obtained from the Health Research Authority (HRA)

Acknowledgements:

MB was funded by the EPSRC-funded UCL Centre for Doctoral Training in Medical Imaging (EP/L016478/1) and the Department of Health's NIHR-funded Biomedical Research Centre at University College London Hospitals. YB was funded by the MRC and Spinal Research Charity through the ERA-NET Neuron joint call (MR/R000050/1). PN was funded by the Wellcome Trust and the NIHR UCLH Biomedical Research Centre. MB and JA were funded by the EU Human Brain Project's Grant Agreement No 785907 (SGA2).

References

References

Adduru, V. R., Michael, A. M., Helguera, M., Baum, S. A., Moore, G. J., 2017. Leveraging clinical imaging archives for radiomics: Reliability of automated methods for brain volume measurement. Radiology 284 (3), 862–869.

Adler, J., Öktem, O., 2018. Learned primal-dual reconstruction. IEEE transactions on medical imaging 37 (6), 1322–1332.

Aganj, I., Yeo, B. T. T., Sabuncu, M. R., Fischl, B., 2012. On removing interpolation and resampling artifacts in rigid image registration. IEEE Transactions on Image Processing 22 (2), 816–827.

Aja-Fernández, S., Tristán-Vega, A., 2013. A review on statistical noise models for magnetic resonance imaging. LPI, ETSI Telecomunicacion, Universidad de Valladolid, Spain, Tech. Rep.

Alexander, D. C., Zikic, D., Zhang, J., et al., 2014. Image quality transfer via random forest regression: applications in diffusion MRI. In: MICCAI. Springer, pp. 225–232.

Ashburner, J., 2007. A fast diffeomorphic image registration algorithm. Neuroimage 38 (1), 95–113.

Ashburner, J., Brudfors, M., Bronik, K., Balbastre, Y., 2019. An algorithm for learning shape and appearance models without annotations. Medical image analysis 55, 197.

Ashburner, J., Friston, K. J., 2000. Voxel-based morphometry—the methods. Neuroimage 11 (6), 805–821.

Ashburner, J., Friston, K. J., 2005. Unified segmentation. Neuroimage 26 (3), 839–851.

Ashburner, J., Ridgway, G. R., 2013. Symmetric diffeomorphic modeling of longitudinal structural MRI. Frontiers in neuroscience 6, 197.

Attias, H., 2000. A variational baysian framework for graphical models. In: Advances in neural information processing systems. pp. 209–215.

Bach, F., Jenatton, R., Mairal, J., Obozinski, G., et al., 2012. Optimization with sparsity-inducing penalties. Foundations and Trends® in Machine Learning 4 (1), 1–106.

Bai, Y., Han, X., Prince, J. L., 2004. Super-resolution reconstruction of MR brain images. In: Proc. of 38th annual conference on information sciences and systems (CISS04). pp. 1358–1363.

Blaiotta, C., Freund, P., Cardoso, M. J., Ashburner, J., 2018. Generative diffeomorphic modelling of large MRI data sets for probabilistic template construction. NeuroImage 166, 117–134.

Boyd, S., Parikh, N., Chu, E., et al., 2011. Distributed optimization and statistical learning via the alternating direction method of multipliers. Found Trends Mach Learning 3 (1), 1–122.

Brudfors, M., Ashburner, J., Nachev, P., Balbastre, Y., Aug 2019. Empirical Bayesian Mixture Models for Medical Image Translation. arXiv e-prints, arXiv:1908.05926.

Brudfors, M., Balbastre, Y., Ashburner, J., 2019. Nonlinear markov random fields learned via backpropagation. In: International Conference on Information Processing in Medical Imaging. Springer, pp. 805–817.

Brudfors, M., Balbastre, Y., Nachev, P., Ashburner, J., 2018. MRI Super-Resolution using Multi-Channel Total Variation. In: MIUA. Southampton, UK.

Cengiz, S., Valdes-Hernandez, M. d. C., Ozturk-Isik, E., 2017. Super resolution convolutional neural networks for increasing spatial resolution of 1H magnetic resonance spectroscopic imaging. In: Annual Conference on Medical Image Understanding and Analysis. Springer, pp. 641–650.

Chatnuntawech, I., Martin, A., Bilgic, B., Setsompop, K., Adalsteinsson, E., Schiavi, E., 2016. Vectorial total generalized variation for accelerated multi-channel multi-contrast MRI. Magnetic resonance imaging 34 (8), 1161–1170.

Chen, Y., Shi, F., Christodoulou, A. G., Xie, Y., Zhou, Z., Li, D., 2018. Efficient and accurate MRI super-resolution using a generative adversarial network and 3D multi-Level densely connected network. In: International Conference on Medical Image Computing and Computer-Assisted Intervention. Springer, pp. 91–99.

Chun, I. Y., Fessler, J. A., 2017. Convolutional dictionary learning: Acceleration and convergence. IEEE Transactions on Image Processing 27 (4), 1697–1712.

Cole, J. H., Poudel, R. P., Tsagkrasoulis, D., Caan, M. W., Steves, C., Spector, T. D., Montana, G., 2017. Predicting brain age with deep learning from raw imaging data results in a reliable and heritable biomarker. NeuroImage 163, 115–124.

Coupé, P., Manjón, J. V., Chamberland, M., Descoteaux, M., Hiba, B., 2013. Collaborative patch-based super-resolution for diffusion-weighted images. NeuroImage 83, 245–261.

Dalca, A. V., Bouman, K. L., Freeman, W. T., Rost, N. S., Sabuncu, M. R., Golland, P., 2018. Medical Image Imputation from Image Collections. IEEE transactions on medical imaging.

Dalca, A. V., Yu, E., Golland, P., Fischl, B., Sabuncu, M. R., Iglesias, J. E., 2019. Unsupervised deep learning for Bayesian brain MRI segmentation. arXiv preprint arXiv:1904.11319.

Daubechies, I., DeVore, R., Fornasier, M., Güntürk, C. S., 2010. Iteratively reweighted least squares minimization for sparse recovery. Communications on Pure and Applied Mathematics: A Journal Issued by the Courant Institute of Mathematical Sciences 63 (1), 1–38.

Dohmatob, E. D., Gramfort, A., Thirion, B., et al., 2014. Benchmarking solvers for TV-ℓ1 least-squares and logistic regression in brain imaging. In: PRNI. IEEE, pp. 1–4.

Fischl, B., Salat, D. H., Van Der Kouwe, A. J., Makris, N., Ségonne, F., Quinn, B. T., Dale, A. M., 2004. Sequence-independent segmentation of magnetic resonance images. Neuroimage 23, S69–S84.

Gholipour, A., Estroff, J. A., Warfield, S. K., 2010. Robust super-resolution volume reconstruction from slice acquisitions: application to fetal brain MRI. IEEE transactions on medical imaging 29 (10), 1739–1758.

Greenspan, H., Peled, S., Oz, G., Kiryati, N., 2001. MRI inter-slice reconstruction using super-resolution. In: International Conference on Medical Image Computing and Computer-Assisted Intervention. Springer, pp. 1204–1206.

Grohs, P., Sprecher, M., 2016. Total variation regularization on Riemannian manifolds by iteratively reweighted minimization. In: Information and Inference. Vol. 4. pp. 353–378.

Gudbjartsson, H., Patz, S., 1995. The Rician distribution of noisy MRI data. Magnetic resonance in medicine 34 (6), 910–914.

He, T., Kong, R., Holmes, A., Nguyen, M., Sabuncu, M., Eickhoff, S. B., Bzdok, D., Feng, J., Yeo, B. T., 2018. Do deep neural networks outperform kernel regression for functional connectivity prediction of behavior? BioRxiv, 473603.

Hestenes, M. R., Stiefel, E., 1952. Methods of conjugate gradients for solving linear systems. Vol. 49. NBS Washington, DC.

Huang, T., Yang, J., 2010. Image super-resolution: Historical overview and future challenges. In: Super-resolution imaging. CRC Press, pp. 19–52.

Jog, A., Carass, A., Prince, J. L., 2014. Improving magnetic resonance resolution with supervised learning. In: Biomedical Imaging (ISBI), 2014 IEEE 11th International Symposium on. IEEE, pp. 987–990.

Jog, A., Carass, A., Prince, J. L., 2016. Self super-resolution for magnetic resonance images. In: International Conference on Medical Image Computing and Computer-Assisted Intervention. Springer, pp. 553–560.

Kainz, B., Steinberger, M., Wein, W., Kuklisova-Murgasova, M., Malamateniou, C., Keraudren, K., Torsney-Weir, T., Rutherford, M., Aljabar, P., Hajnal, J. V., et al., 2015. Fast volume reconstruction from motion corrupted stacks of 2D slices. IEEE transactions on medical imaging 34 (9), 1901–1913.

Kamnitsas, K., Ledig, C., Newcombe, V. F., Simpson, J. P., Kane, A. D., Menon, D. K., Rueckert, D., Glocker, B., 2017. Efficient multi-scale 3D CNN with fully connected CRF for accurate brain lesion segmentation. Medical image analysis 36, 61–78.

Klöppel, S., Stonnington, C. M., Chu, C., Draganski, B., Scahill, R. I., Rohrer, J. D., Fox, N. C., Jack Jr, C. R., Ashburner, J., Frackowiak, R. S., 2008. Automatic classification of MR scans in Alzheimer's disease. Brain 131 (3), 681–689.

Litjens, G., Kooi, T., Bejnordi, B. E., Setio, A. A. A., Ciompi, F., Ghafoorian, M., Van Der Laak, J. A., Van Ginneken, B., Sánchez, C. I., 2017. A survey on deep learning in medical image analysis. Medical image analysis 42, 60–88.

Liu, H., Michel, E., Casey, S. O., Truwit, C. L., 2002. Actual imaging slice profile of 2D MRI. In: Medical Imaging 2002: Physics of Medical Imaging. Vol. 4682. International Society for Optics and Photonics, pp. 767–773.

Manjón, J. V., Coupé, P., Buades, A., et al., 2010a. MRI superresolution using self-similarity and image priors. Int J Biomed Imag 2010, 17.

Manjón, J. V., Coupé, P., Buades, A., et al., 2010b. Non-local MRI upsampling. Med Image Anal 14 (6), 784–792.

Miller, K. L., Alfaro-Almagro, F., Bangerter, N. K., Thomas, D. L., Yacoub, E., Xu, J., Bartsch, A. J., Jbabdi, S., Sotiropoulos, S. N., Andersson, J. L., et al., 2016. Multimodal population brain imaging in the UK Biobank prospective epidemiological study. Nature neuroscience 19 (11), 1523.

Monté-Rubio, G. C., Falcón, C., Pomarol-Clotet, E., Ashburner, J., 2018. A comparison of various MRI feature types for characterizing whole brain anatomical differences using linear pattern recognition methods. NeuroImage 178, 753–768.

Ollier, W., Sprosen, T., Peakman, T., 2005. UK Biobank: from concept to reality.

Palmer, L. J., 2007. UK Biobank: bank on it. The Lancet 369 (9578), 1980–1982.

Peeters, R. R., Kornprobst, P., Nikolova, M., Sunaert, S., Vieville, T., Malandain, G., Deriche, R., Faugeras, O., Ng, M., Van Hecke, P., 2004. The use of super-resolution techniques to reduce slice thickness in functional MRI. International Journal of Imaging Systems and Technology 14 (3), 131–138.

Peled, S., Yeshurun, Y., 2001. Super-resolution in MRI: application to human white matter fiber tract visualization by diffusion tensor imaging. Magnetic Resonance in Medicine: An Official Journal of the International Society for Magnetic Resonance in Medicine 45 (1), 29–35.

Pham, C.-H., Ducournau, A., Fablet, R., Rousseau, F., 2017. Brain MRI super-resolution using deep 3D convolutional networks. In: Biomedical Imaging (ISBI 2017), 2017 IEEE 14th International Symposium on. IEEE, pp. 197–200.

Plenge, E., Poot, D. H., Bernsen, M., Kotek, G., et al., 2012. Super-resolution methods in MRI: Can they improve the trade-off between resolution, signal-to-noise ratio, and acquisition time? Magn Reson Med 68 (6), 1983–1993.

Plenge, E., Poot, D. H., Niessen, W. J., Meijering, E., 2013. Super-resolution reconstruction using cross-scale self-similarity in multi-slice MRI. In: International Conference on Medical Image Computing and Computer-Assisted Intervention. Springer, pp. 123–130.

Poot, D. H., Van Meir, V., Sijbers, J., 2010. General and efficient super-resolution method for multi-slice MRI. In: International conference on medical image computing and computer-assisted intervention. Springer, pp. 615–622.

Reuter, M., Schmansky, N. J., Rosas, H. D., Fischl, B., 2012. Within-subject template estimation for unbiased longitudinal image analysis. Neuroimage 61 (4), 1402–1418.

Roobottom, C., Mitchell, G., Morgan-Hughes, G., 2010. Radiation-reduction strategies in cardiac computed tomographic angiography. Clinical radiology 65 (11), 859–867.

Rousseau, F., Initiative, A. D. N., et al., 2010a. A non-local approach for image super-resolution using intermodality priors. Medical image analysis 14 (4), 594–605.

Rousseau, F., Kim, K., Studholme, C., Koob, M., Dietemann, J.-L., 2010b. On super-resolution for fetal brain MRI. In: International Conference on Medical Image Computing and Computer-Assisted Intervention. Springer, pp. 355–362.

Rudin, L. I., Osher, S., Fatemi, E., 1992. Nonlinear total variation based noise removal algorithms. Physica D: nonlinear phenomena 60 (1-4), 259–268.

Rueda, A., Malpica, N., Romero, E., 2013. Single-image super-resolution of brain MR images using overcomplete dictionaries. Medical image analysis 17 (1), 113–132.

Sapiro, G., Ringach, D. L., 1996. Anisotropic diffusion of multivalued images with applications to color filtering. IEEE T Image Process 5 (11), 1582–1586.

Schrouff, J., Rosa, M. J., Rondina, J. M., Marquand, A. F., Chu, C., Ashburner, J., Phillips, C., Richiardi, J., Mourao-Miranda, J., 2013. PRoNTo: pattern recognition for neuroimaging toolbox. Neuroinformatics 11 (3), 319–337.

Shi, F., Cheng, J., Wang, L., Yap, P.-T., Shen, D., 2015. LRTV: MR image super-resolution with low-rank and total variation regularizations. IEEE transactions on medical imaging 34 (12), 2459–2466.

Shilling, R. Z., Robbie, T. Q., Bailloeul, T., Mewes, K., Mersereau, R. M., Brummer, M. E., 2009. A super-resolution framework for 3-D high-resolution and high-contrast imaging using 2-D multislice MRI. IEEE transactions on medical imaging 28 (5), 633–644.

Sindel, A., Breininger, K., Käßer, J., Hess, A., Maier, A., Köhler, T., 2018. Learning from a Handful Volumes: MRI Resolution Enhancement with Volumetric Super-Resolution Forests. arXiv preprint arXiv:1802.05518.

Smith, S. M., Nichols, T. E., 2018. Statistical challenges in "Big Data" human neuroimaging. Neuron 97 (2), 263–268.

Smith, S. M., Vidaurre, D., Alfaro-Almagro, F., Nichols, T. E., Miller, K. L., 2019. Estimation of brain age delta from brain imaging. NeuroImage.

Tanno, R., Worrall, D. E., Ghosh, A., Kaden, E., Sotiropoulos, S. N., Criminisi, A., Alexander, D. C., 2017. Bayesian image quality transfer with cnns: Exploring uncertainty in dmri super-resolution. In: International Conference on Medical Image Computing and Computer-Assisted Intervention. Springer, pp. 611–619.

Tourbier, S., Bresson, X., Hagmann, P., Thiran, J.-P., Meuli, R.,

Cuadra, M. B., 2015. An efficient total variation algorithm for super-resolution in fetal brain MRI with adaptive regularization. NeuroImage 118, 584–597.

Van Essen, D. C., Smith, S. M., Barch, D. M., Behrens, T. E., Yacoub, E., Ugurbil, K., Consortium, W.-M. H., et al., 2013. The WU-Minn human connectome project: an overview. Neuroimage 80, 62–79.

Van Reeth, E., Tham, I. W., Tan, C. H., et al., 2012. Super-resolution in magnetic resonance imaging: A review. Concepts Magn Reson 40 (6), 306–325.

Yang, J., Yin, W., Zhang, Y., Wang, Y., 2009. A fast algorithm for edge-preserving variational multichannel image restoration. SIAM J Imaging Sci 2 (2), 569–592.

Yue, L., Shen, H., Li, J., Yuan, Q., Zhang, H., Zhang, L., 2016. Image super-resolution: The techniques, applications, and future. Signal Processing 128, 389–408.

Zhang, X., Lam, E. Y., Wu, E. X., Wong, K. K., 2008. Application of Tikhonov regularization to super-resolution reconstruction of brain MRI images. In: Medical imaging and informatics. Springer, pp. 51–56.

Zhang, Y., Brady, M., Smith, S., 2001. Segmentation of brain MR images through a hidden Markov random field model and the expectation-maximization algorithm. IEEE Trans Med Imag 20 (1), 45–57.

Zhao, C., Carass, A., Dewey, B. E., Woo, J., Oh, J., Calabresi, P. A., Reich, D. S., Sati, P., Pham, D. L., Prince, J. L., 2018. A deep learning based anti-aliasing self super-resolution algorithm for MRI. In: International Conference on Medical Image Computing and Computer-Assisted Intervention. Springer, pp. 100–108.

Zheng, H., Qu, X., Bai, Z., Liu, Y., Guo, D., Dong, J., Peng, X., Chen, Z., 2017. Multi-contrast brain magnetic resonance image super-resolution using the local weight similarity. BMC medical imaging 17 (1), 6.